The Astrophysical Journal, 851:3 (10pp), 2017 December 10 https://doi.org/10.3847/1538-4357/aa9706

Contribution of Field Strength Gradients to the Net Vertical Current of Active Regions

P. Vemareddy
Indian Institute of Astrophysics, Koramangala, Bengaluru-560 034, India; vemareddy@iiap.res.in
Received 2017 September 18; revised 2017 October 23; accepted 2017 October 28; published 2017 December 5

Abstract

We examined the contribution of field strength gradients for the degree of net vertical current (NVC) neutralization in active regions (ARs). We used photospheric vector magnetic field observations of AR 11158 obtained by *Helioseismic and Magnetic Imager* on board *SDO* and *Hinode*. The vertical component of the electric current is decomposed into twist and shear terms. The NVC exhibits systematic evolution owing to the presence of the sheared polarity inversion line between rotating and shearing magnetic regions. We found that the sign of shear current distribution is opposite in dominant pixels (60%–65%) to that of twist current distribution, and its time profile bears no systematic trend. This result indicates that the gradient of magnetic field strength contributes to an opposite signed, though smaller in magnitude, current to that contributed by the magnetic field direction in the vertical component of the current. Consequently, the net value of the shear current is negative in both polarity regions, which when added to the net twist current reduces the direct current value in the north ($B_z > 0$) polarity, resulting in a higher degree of NVC neutralization. We conjecture that the observed opposite signs of shear and twist currents are an indication, according to Parker, that the direct volume currents of flux tubes are canceled by their return currents, which are contributed by field strength gradients. Furthermore, with the increase of spatial resolution, we found higher values of twist, shear current distributions. However, the resolution effect is more useful in resolving the field strength gradients, and therefore suggests more contribution from shear current for the degree of NVC neutralization.

Key words: Sun: coronal mass ejections (CMEs) – Sun: evolution – Sun: fundamental parameters – Sun: magnetic fields – Sun: photosphere – Sun: sunspots

1. Introduction

Electric currents in the astrophysical plasmas are generated by the distortion of the magnetic field by external forces applied by field-free plasma (Parker 1979). These local distortions of the local magnetic field result in local sources of the electric current. In the Sun, these currents enter the corona through embedded emerging magnetic fields from the convection zone through the photosphere. Despite their generation mechanisms, these currents are believed to play a vital role in magnetic solar eruptions. Dissipation of these electrical currents during reconnection is an explained mechanism of releasing magnetic energy to thermal and kinetic energy during the transient activity of the Sun. However, the Parkers theoretical prediction (Parker 1996) of neutralized net current over a cross-section of the flux tube at the photosphere is inconsistent with their role in eruptions.

As per Parker (1996), the presence of volume currents in twisted magnetic fibrils embedded in a relatively field-free space occupied by fluid plasma, necessarily implies the existence of return surface (sheath) currents at the boundaries of these photospheric fibrils. As this is obviously the case for the photosphere, the net current obtained by summing over the cross-section of the flux bundle from an isolated magnetic polarity region should yield to a vanishing value. Using the high-resolution vector magnetic field observations, this prediction was found to be nearly satisfied (Venkatakrishnan & Tiwari 2009) in many isolated sunspot regions of active regions (ARs).

In many studied ARs (Ravindra et al. 2011; Georgoulis et al. 2012; Vemareddy et al. 2015), however, the observance of the non-neutralized net current is in need of a proper explanation. The presence of a strong sheared neutral line amid the compact polarity regions is one of the main contributors to the observed net current (Falconer 2001; Vemareddy et al. 2015) through the line integral of Biot Savarts law around a polarity flux region. In the case of well-isolated sunspot regions, the missing surface (sheath) current due to the limited resolution of the magnetogram is suggested to be the predominant contributor to the net amount of the vertical current.

The breakdown of the net current neutralization has implications on CME activity in the AR. The hoop force of the CME flux rope is proportional to the square of the net current in the flux rope channel (Zakharov & Shafranov 1986), which is the algebraic sum of the net direct current (DC) and the return current (RC). The equilibrium and stability properties of the flux rope then requires the neutralization of the net current for which hoop force vanishes. Numerical simulations indicate that a major breakdown occurs during emerging phase of AR (Török et al. 2014), during which opposite polarity regions are compact with a sheared PIL. Observational studies also confirm that the sheared PIL is a major contributor to DC and proposed the degree of current neutralization as the proxy for assessing the ability of ARs to produce CMEs (Liu et al. 2017). Although DC has origins of volumetric currents, it is not fully understood how and to what extent the RC is organized around the DC channel for a given degree of current neutralization.

The sheath (return) current is associated with the field-free plasma, surrounding the flux bundle and is opposite in sign to that of the volume (direct) current of the flux bundle. According to the differential form of Ampere's law, the electric current can be written as

$$\boldsymbol{J} = \frac{1}{\mu_0}\nabla \times \boldsymbol{B}, \tag{1}$$

where $\mu_0 = 4\pi \times 10^{-7} Henry$[1] per meter, and $\boldsymbol{J}$ has units of Ampere (A) per square meter. Writing $\boldsymbol{B} = B\boldsymbol{b}$ with $\boldsymbol{b}$ as the unit vector along the direction of the magnetic field, the current $\boldsymbol{J}$ can then be decomposed into two terms (Zhang 2001):

$$\boldsymbol{J} = \frac{B}{\mu_0}\nabla \times \boldsymbol{b} + \frac{1}{\mu_0}\nabla B \times \boldsymbol{b}. \quad (2)$$

The first term in the above equation includes currents both perpendicular and parallel to the field and is essentially related to the twist of magnetic field lines. The latter is due to the gradient of magnetic field strength across the field direction and is strongly contributed from complex magnetic fields with strong inhomogeneities across the field lines. This term essentially contributes to cross-field currents. We denote the first term, after Zhang (2001), as the twist/chiral current density $\boldsymbol{J}_{\rm ch}$ and the second term as the shear current density $\boldsymbol{J}_{\rm sh}$. Furthermore, in the case of a flux tube, the Lorentz force due to these cross-field currents is mainly due to magnetic pressure and tends to expand the flux tube against the external nonmagnetized plasma pressure that keeps the flux tube together.

The return (sheath) current is expected to peak on the surface of the flux tube, where the interface between the magnetized and field-free plasma media occurs (Georgoulis et al. 2012). This provides us with the clue that the return (sheath) current is related to a gradient of the fields and is likely contributed from the shear current ($\boldsymbol{J}_{\rm sh}$). The distribution, sign, and magnitude of $\boldsymbol{J}_{\rm sh}$ are not well studied in the literature. This needs supportive evidence for the assuption that the quantity, which is of opposite and equal magnitude, to the volume current is related to the shear current.

With the now available uninterrupted vector magnetic field observations, we can only calculate the vertical component of $\boldsymbol{J}_{\rm sh}$. $\boldsymbol{J}_{\rm sh}$ adds to the perpendicular component of $\boldsymbol{J}_{\rm ch}$ to give a total cross-field current. In a purely force-free field, the net value of the cross-field current, however, is zero. In the present work, we verified that the sign and amount of the vertical component of the $\boldsymbol{J}_{\rm sh}$ current distribution (mainly contributes to sheath) are as expected from the Parkers theoretical prediction. The net vertical current (NVC) is decomposed to shear and twist terms, and we analyzed their spatial distribution and time evolution using continuous time series vector magnetic field observations at the photosphere.

We arranged the contents of this manuscript as follows. In Section 2, we describe the data sets and decomposition procedure of the vertical current. Results of the observational analysis are presented in Section 3. A discussion of the results is given in Section 4 and summarized in Section 5.

2. Data Sets and Numerical Procedure

In this study of the evolution of the net current and its decomposed terms, we used high time resolution vector magnetic observations of AR patch NOAA 11158, obtained from the *Helioseismic and Magnetic Imager* (HMI, Schou et al. 2012) on board the *Solar Dynamics Observatory*. The vector magnetic field in the AR patch is deduced after a pipelined procedure of stokes vector inversion and ambiguity resolution (Borrero et al. 2011; Bobra et al. 2014; Hoeksema et al. 2014). These disambiguated vector observations of the AR patch in the native coordinate system (latitude, longitude) are remapped to disk center by the cylindrical equal area projection method such that the AR patch center matches the disk center. This is a spherical transformation, accounting for the foreshortening effect, and the final image of the AR patch appears as if one is observing directly overhead (Calabretta & Greisen 2002). The field vectors are then transformed to the heliocentric spherical coordinate system, resulting in (B_r, B_θ, B_ϕ), which are provided as a `hmi.sharp_cea_720s` data product. According to Gary & Hagyard (1990), the field components (B_r, B_θ, B_ϕ) in heliocentric spherical coordinates are identical to (B_z, $-B_y$, B_x) in heliographic coordinates (see the appendix section in Sun 2013), which are suitable for various studies in Cartesian coordinates.

With the observations of vector magnetograms, we can only compute the vertical component of current density distribution (see Equation (1)):

$$\begin{aligned} Jz &= \frac{1}{\mu_0}\left(\frac{\partial B_y}{\partial x} - \frac{\partial B_x}{\partial y}\right) \\ &= \frac{B}{\mu_0}\left(\frac{\partial b_y}{\partial x} - \frac{\partial b_x}{\partial y}\right) + \frac{1}{\mu_0}\left(b_y\frac{\partial B}{\partial x} - b_x\frac{\partial B}{\partial y}\right) \\ &= Jz_{\rm ch} + Jz_{\rm sh}. \end{aligned} \quad (3)$$

For the sake of brevity, here onwards, we refer to $Jz_{\rm ch}$ as the twist current and $Jz_{\rm sh}$ as the shear current. The partial derivatives are approximated by the finite differencing scheme employing a three-point Lagrangian interpolation polynomial (Chapter 3 in Hildebrand 1974). The most common way of computing a numerical derivative of a function $f(x)$ at any point is to approximate $f(x)$ by a polynomial. Interpolation at any point p on a function $f(x)$ can be obtained by constructing a lowest-degree Lagrange polynomial that fits each given point $f(x_i)$ corresponding to x_i. From these interpolating polynomials, the numerical differentiation of $f(x)$ on a consecutive three-point $((x_{-1}, f(x_{-1})), (x_0, f(x_0)), (x_1, f(x_1))$ stencil with error is given by

$$\begin{aligned} f'(x_j) = {} & f(x_{-1})\left[\frac{2x_j - x_0 - x_1}{(x_{-1} - x_0)(x_{-1} - x_1)}\right] \\ & + f(x_0)\left[\frac{2x_j - x_{-1} - x_1}{(x_0 - x_{-1})(x_0 - x_1)}\right] \\ & + f(x_1)\left[\frac{2x_j - x_{-1} - x_0}{(x_1 - x_{-1})(x_1 - x_0)}\right] \\ & + \frac{f^{(3)}(\xi(x))}{6}\prod_{k=-1,k\neq j}^{1}(x_j - x_k) \end{aligned} \quad (4)$$

to a second-order accuracy. For equally spaced points of h ($x_0 = x_{-1} + h$; $x_1 = x_{-1} + 2h$), this reduces to the central difference formula $f'(x_j) = \frac{1}{2h}[-f(x_{-1}) + f(x_1)]$. Similarly, higher stencils are used for higher accuracy. For a five-point stencil, the central difference formula becomes $f'(x_j) = \frac{f(x_{-2}) - 8f(x_{-1}) + 8f(x_1) - f(x_2)}{2h}$. However, stencils with more points introduce oscillations at the edges of an interval. In addition to noise in the data, this problem suggests generally that one should use the three-point stencil.

[1] 1 Henry = kg m^2 s^{-2} A^{-2}.

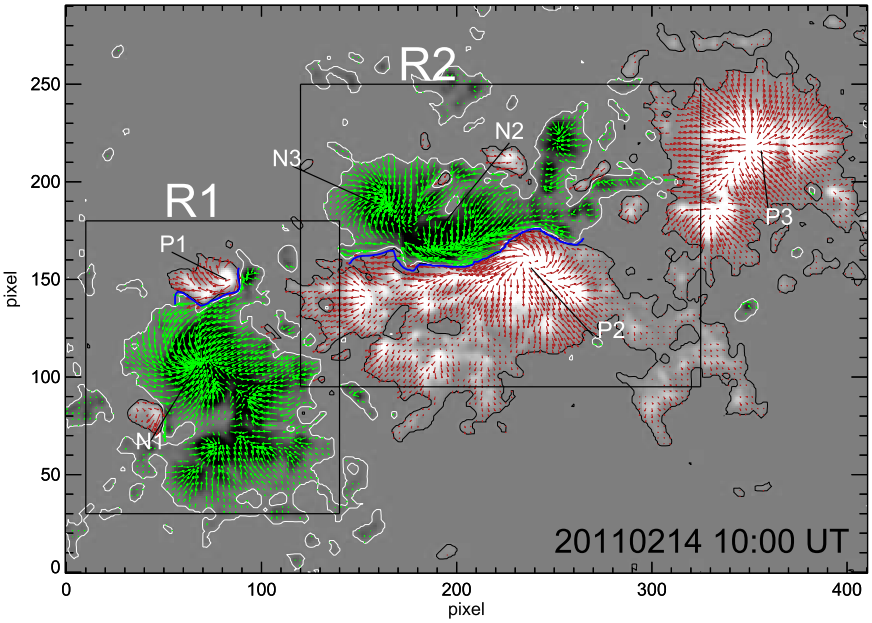

Figure 1. Typical HMI vector magnetogram of AR 11158 at 10:00UT on 2011 February 14. The horizontal field vectors in red (green) are overplotted on the vertical component of the magnetic field map with isocontours at 50 G (−50 G) in black (white). The dominant sunspot polarities are marked as P/N* within the rectangular regions of interest R1 and R2 (subregions) for further correspondence. The blue solid curves represent the strongly sheared (with shear angle greater than 45°) PILs separating major positive and negative vertical flux regions. The field of view is 207 × 146 arcsec^2.

From these distributions of current densities, the net current and its constituting components,

$$I = \sum_{i=1}^{N} Jz_i; \quad I_{\rm ch} = \sum_{i=1}^{N} (Jz_{\rm ch})_i; \quad I_{\rm sh} = \sum_{i=1}^{N} (Jz_{\rm sh})_i \qquad (5)$$

are computed by summing N pixels over a region of interest. The errors due to the field measurements and inversion procedure accumulate to yield the uncertainty of their values in a range. The given estimated errors in the vertical component vary by about 40 G and in horizontal components by 80 G. For the sake of avoiding inconsistent results as well as to stabilize the time evolution profile of the net current due to these uncertainties, we account for the pixels having threshold values $|B_{\rm tot}| > 150$ G in all of the above calculations.

3. Results

3.1. Distribution of Jz, Jz_{ch}, and Jz_{sh}

The vector magnetogram of AR 11158 is shown in Figure 1. This AR emerged on 2013 February 11, and continued to emerge until February 13 with increasing area of the individual sunspots and finally resulting in a large and complex AR. During this phase of evolution, the sunspots (positive polarity P1, P2, P3 and negative polarity of N1, N2, N3) show proper motions and the interface among them forms a sheared polarity inversion line (PIL), which is obvious from the orientation of horizontal vectors. The AR is divided into two subregions (R1 and R2) with strongly shared PIL and were the sources of significant activity (Vemareddy et al. 2012a, 2012b). In particular, R1 is dominated by sunspot rotation, whereas shear motion is predominant in R2.

The distribution of vertical current density along with its shear ($Jz_{\rm sh}$) and twist ($Jz_{\rm ch}$) components are plotted in Figure 2 at different epochs of AR evolution. The values of Jz are spread over a wide range of the entire AR with a typical maximum value of 200 mAm^{-2} in magnitude in both polarities. In particular, an intense distribution with large values is located about the interface of P1 and N2 in R1, and P2 and N2 in R2. The positive (negative) polarity P1 (N1) has a dominant negative (positive) current distribution. Similarly, in R2, positive (negative) polarity P3 is with dominantly positive (negative) distribution of Jz.

The distribution of $Jz_{\rm ch}$ closely matches with the Jz, whereas the morphology of both $Jz_{\rm ch}$ and Jz are quite different from $Jz_{\rm sh}$. Furthermore, in the given scaling, the large values of Jz, $Jz_{\rm ch}$ are located around PIL regions, whereas $Jz_{\rm sh}$ is always smaller in magnitude, while its sign is opposite to that of $Jz_{\rm ch}$ in a majority of pixels. We highlight these prominent locations by marking them with yellow arrows in the Figure 2.

For displaying the trend of how many of the pixels have opposite signs of twist and shear current, we obtain the signs in both $Jz_{\rm ch}$ and $Jz_{\rm sh}$ maps and multiply these signed maps to further examine the nature of the sign distribution. These "sign" maps are plotted in Figure 3 at the same time frames as for the maps shown in Figure 2. Pixels with the same sign in $Jz_{\rm ch}$ and $Jz_{\rm sh}$ maps will show a value of +1 whereas pixels with opposite sign will show a value of −1. Thus the black pixels indicate that $Jz_{\rm sh}$ and $Jz_{\rm ch}$ have opposite signs. This procedure is applied for different time frames and inferred that about two-thirds of pixels have oppositely signed $Jz_{\rm sh}$ and $Jz_{\rm ch}$. They were located all over the active region without clustering to a specific location. We also checked this inference by computing the current maps with a five-point stencil and noted the difference limited to less than 1%.

In a similar way, we followed the same procedure for Jz and the $Jz_{\rm ch}$, and the corresponding signed maps are displayed in Figure 4. In this case, we found that two-thirds (one-third) of the pixels have the same (opposite) signed values. We note that these opposite signed pixels are located mostly in the outside regions of sunspot polarities.

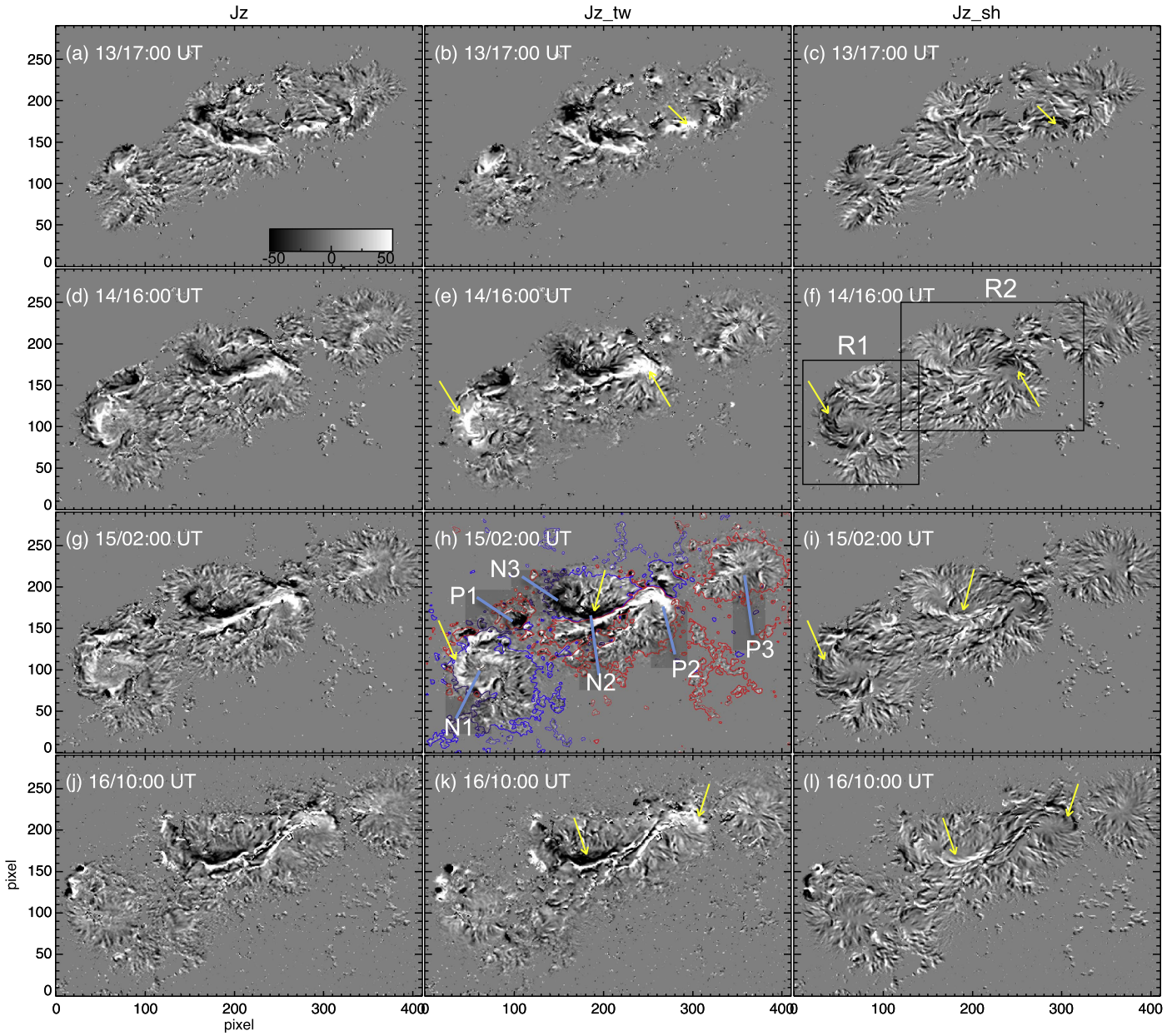

Figure 2. Distribution of vertical current (Jz, First column), chiral/twist current (Jz_{ch}, second column), and shear current (Jz_{sh}, third column) at different epochs of evolution in AR 11158. Note that the distributions of Jz and Jz_{ch} are similar in almost every location. Identically oriented arrows (yellow) refer to prominent (few to notify) opposite polarity distribution patches of Jz_{ch} and Jz_{sh} currents in respective panels at a given time. Contours ($\pm$100 G) of the LOS magnetic field are plotted in panel (h) with labeled sunspot regions and the regions of interest for further analysis are shown in panel (f) with rectangles. All of these maps are scaled within $\pm$50 mAm^{-2} as indicated in panel (a). The FOV in each panel is the same as in Figure 1.

3.2. Evolution of I, I_{ch}, and I_{sh}

Next, the I, I_{ch}, and I_{sh} are evaluated at individual north ($B_z > 0$) and south ($B_z < 0$) polarities in the entire AR, R1, and R2 separately and their time evolution is plotted in Figure 5's panels. The profile of I indicates systematic evolution in both the polarities according to the PIL shear generated by shearing and rotation motions (see Vemareddy et al. 2015 for a detailed discussion). Particularly, the J-shaped current patterns contribute up to 80% of the net value in each polarity. The I_{ch} of the vertical current, on the other hand, behaves very much like the NVC and evolves in step with the rotation rate of the rapidly rotating sunspot N1, first evaluated in Vemareddy et al. (2012a), and later elaborated on in Vemareddy et al. (2015). In total, the I_{ch} profile in each signed flux region resembles that of the I, i.e., I_{ch} in north (south) polarity in R1 (R2, entire AR) had a similar trend to that of the net current in north (south) polarity in R1 (R2, entire AR). This is consistent with the statistics that two-thirds of Jz_{ch} pixels have the same signed values as those of the Jz distribution.

The magnitude of I_{sh} in any polarity region is smaller compared to I_{ch} and exhibits no correlated trend with I_{ch}. It can be noted that the I_{sh} in R2 sub-region is negative to that of the I_{ch} at each polarity. However, it remains negative in both of the polarities when considered in the entire AR. Owing to the fact

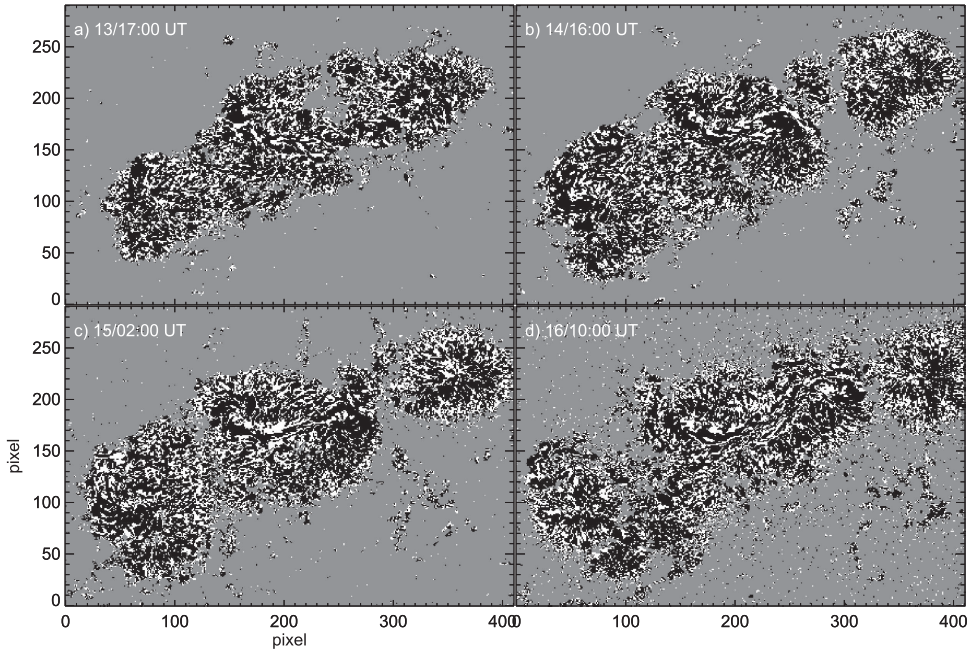

Figure 3. Maps showing a relative sign distribution of Jz_{ch} and Jz_{sh}. Black (white) pixels refer to those having opposite (same) signs of Jz_{ch} and Jz_{sh} at a time. Note that opposite signed (about two-thirds of) pixels are greater in number and are distributed all over the AR.

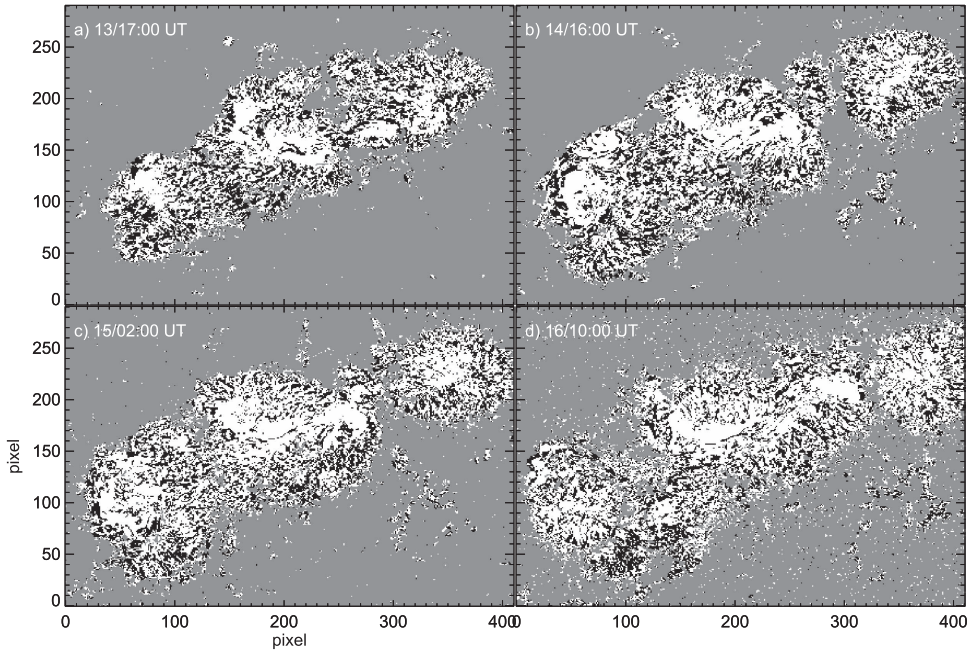

Figure 4. Maps showing the relative sign distribution of Jz and Jz_{ch}. Black (white) pixels refer to those having opposite (same) signs of Jz and Jz_{ch} at a time. Note that the same signed (about two-thirds of) pixels are predominant in number localized in strong field regions.

that the magnitude and sign of I_{sh} is different from I_{ch}, the net current is different from I_{ch}.

3.3. Contribution of I_{sh} in Net Current Neutralization

We now examine the neutralization of the current in each polarity. For that, we obtain the ratio of DC and RC in each polarity (Török et al. 2014). In a given polarity, the current distribution is both positive and negative, and the dominance of either of these signed currents decides the chirality of the magnetic field. Here the DC is the dominant current, and is surrounded by RC as the nondominant current. The ratio |DC/RC| indicates the extent of departure from net current neutralization in any polarity. It is important to point out that the DC is positive at south polarity of R1 and north polarity of R2. In Figure 6, we plot |DC/RC| for Jz in the north (left column panels) and south (right column panels) polarities, following the same format of Figure 5. In all of the regions,

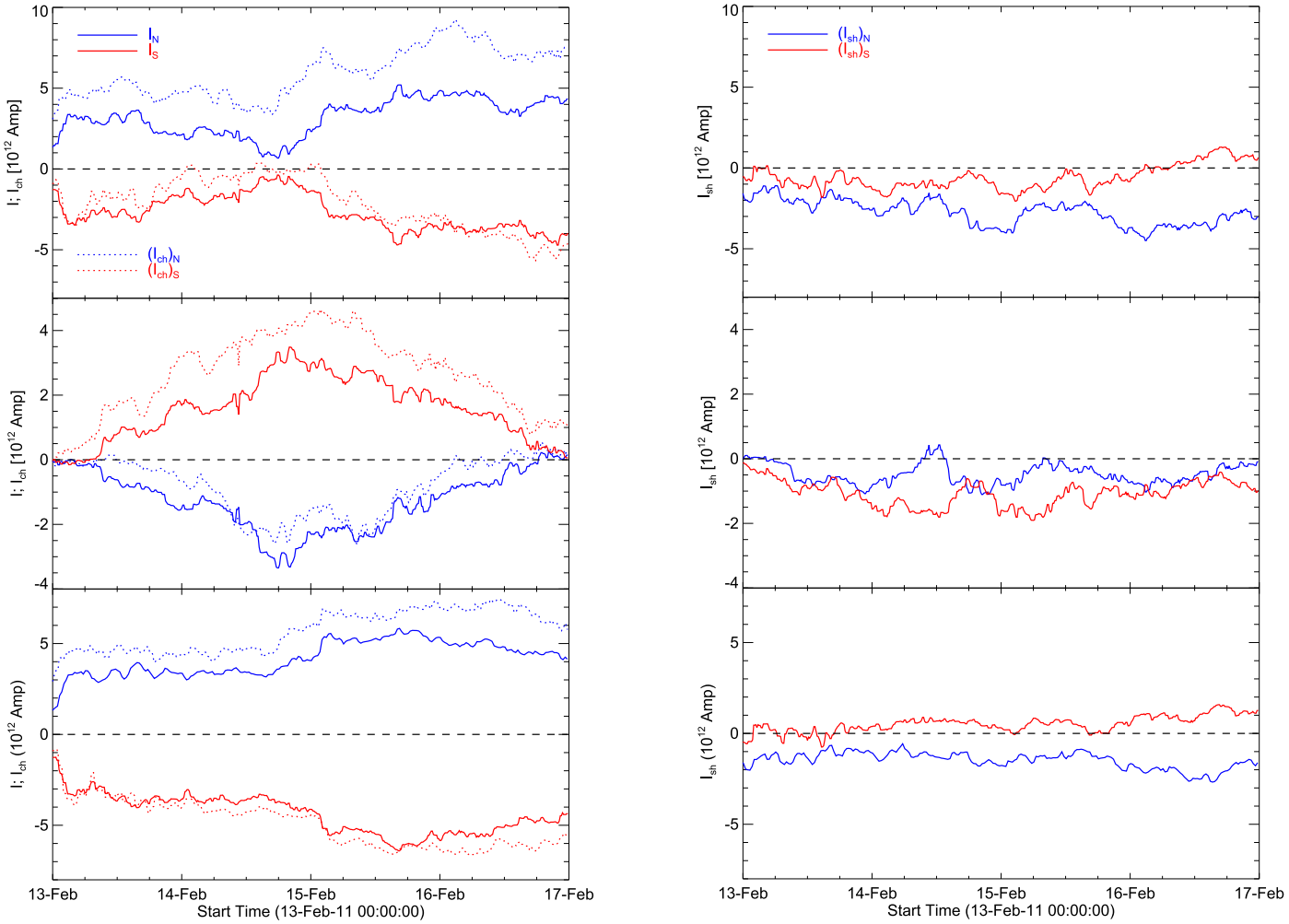

Figure 5. Left column: time evolution of I over the entire AR 11158, sub-region R1, and sub-region R2 in the top, middle, and bottom panels, respectively. Blue (red) corresponds to the integrated value at the north (south) polarity region. I_{ch} is also shown with dotted curves in the respective panels. Right column: time evolution of I_{sh} obtained at individual polarities of the entire AR, R1, and R2 in the top, middle, and bottom panels respectively. Note that the net value of I_{sh} in both polarities is negative from the entire AR.

non-neutralization is well above unity because of volumetric currents from sheared PIL in R1 and R2. An important note is that the DC in R1 is negative and R2 is positive.

Similarly, the |DC/RC| is deduced for Jz_{ch} in each polarity and plotted with dotted curves in the respective panels of Figure 6. Owing to the contribution from I_{sh}, the |DC/RC| curves for Jz_{ch} and Jz are differently deviated from unity. For example, in R2, the I_{sh} is opposite in sign to I_{ch} in each polarity, which increases the numerator (DC) value in both the polarities predominantly resulting in smaller value of |DC/RC| from Jz than Jz_{ch}. In the entire AR, the DC in north polarity and RC in south is reduced by net negative I_{sh}, and yields lower and higher value of |DC/RC| from Jz. It appears that, at least in this AR, the current contribution from field strength gradients is dominantly negative in sign and leads to a lower degree of non-neutralization.

3.4. Current Decomposition in the Hinode Vector Magnetic Field

We also performed the above analysis of NVC decomposition using ultra-high-resolution *Hinode* spectro-polarimetry observations of AR 10930 during 2006 December 8–13. The vector magnetograms are prepared by employing well established techniques described in Ravindra et al. (2011). For an exemplary case, we showed a distribution of Jz and its decomposed components in Figure 7. In particular, the fine zebra patterns observed correspond to penumbral fibrils in the larger negative polarity sunspot. By visual inspection, the umbral region is set by a threshold of $B_z < -2000$ G and the region with B_z between -2000 and -100 G belongs to penumbra. From this segmeted analysis, we found that 18% (82%) of net current comes from the umbral (penumbral) region of this negative polarity. This is consistent with the earlier conclusion in AR 11158 that a major part of the net current belongs to the sheared PIL of interfering sunspot penumbre.

Many locations of the sunspots have opposite signed current distribution, which is clear on a keen comparison of shear and twist current maps. Similar to HMI observations of AR 11158, the evolution of the I_{ch} in AR 11930 closely resembled that of the I with the same sign, while the I_{sh} was smaller than the I_{ch} and had a sign opposite to that of the twist current (Suthar et al. 2014).

In Table 1, we summarized these metrics in our context of study. Importantly, the percentage of opposite signed pixels

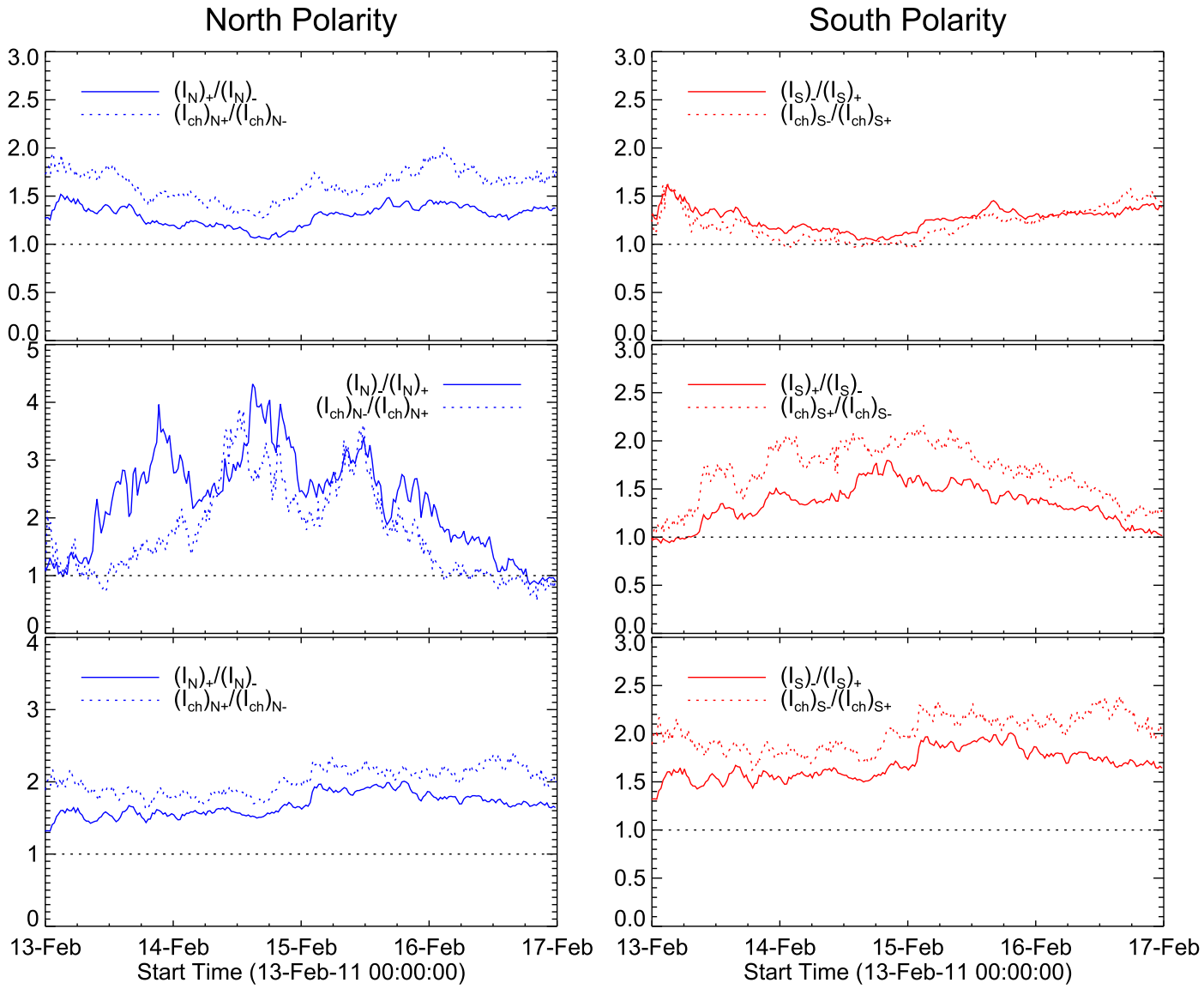

Figure 6. Time evolution of |DC/RC| in the entire AR, sub-region R1, and sub-region R2 in the top, middle, and bottom panels, respectively. The |DC/RC| at the north (south) polarity is plotted in the left (right) column panels. Dotted curves in the respective panels correspond to |DC/RC| from the Jz_{ch} distribution. Owing to the net negative value of I_{sh}, the DC value decreases in the north polarity and increases in the south polarity. Consequently, the |DC/RC| curve of Jz differs from that of Jz_{ch}. The horizontal dashed line in each panel indicates the current neutralization.

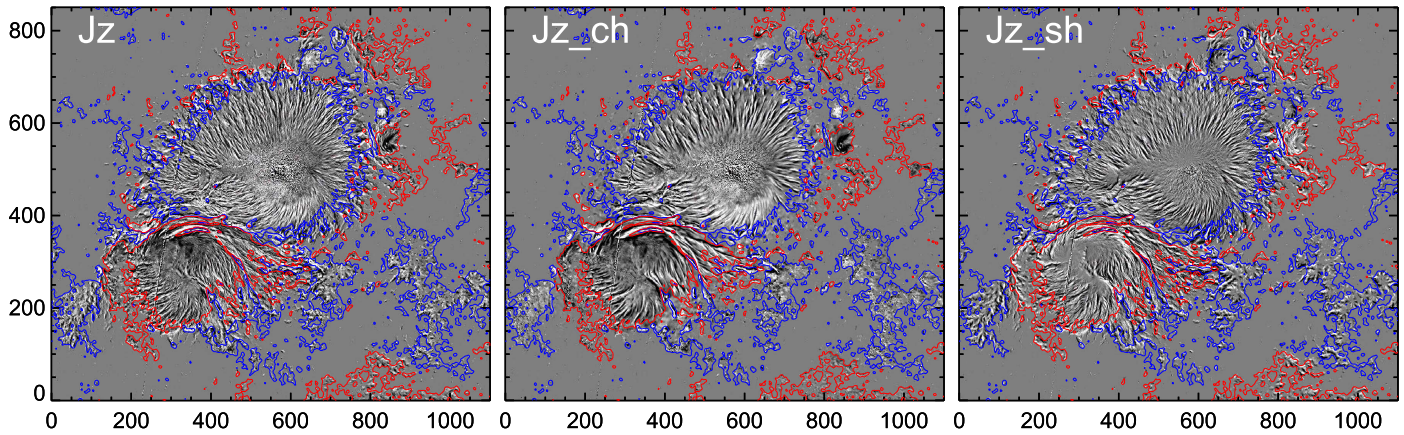

Figure 7. Distribution of Jz, Jz_{ch}, and Jz_{sh} (scaled within ± 80 mAm^{-2}) in AR 10930 on 2006 December 13 at 13:00 UT. The corresponding vector magnetograms at $0\farcs15$ per pixel resolution are derived from spectropolarimetric measurements on board *Hinode*. Contours (blue/red) of vertical magnetic field at ± 130 G are also shown in each panel.

Table 1
Values of Decomposed Net Vertical Current Obtained Using *Hinode* Observations

Date [UT]	Pixel Size (arcsec)	I_N (I_S) (10^{12} A)	$(I_N)_{ch}$ ($(I_S)_{ch}$) (10^{12} A)	$(I_N)_{sh}$ ($(I_S)_{sh}$) (10^{12} A)	% Opposite (Same) sign pixels
2006 Dec 13 04:00	0.3	−7.0 (6.5)	−9.8(8.1)	2.6(−1.5)	62(38)
2006 Dec 13 07:00	0.15	−7.1 (5.4)	−9.8(6.3)	2.6(−0.7)	62(38)
2006 Dec 13 13:00	0.3	−5.8(5.0)	−8.7(6.4)	2.9(−1.4)	60(40)
2006 Dec 13 16:00	0.3	−5.9(5.4)	−8.9(5.6)	2.9(−1.3)	61(39)

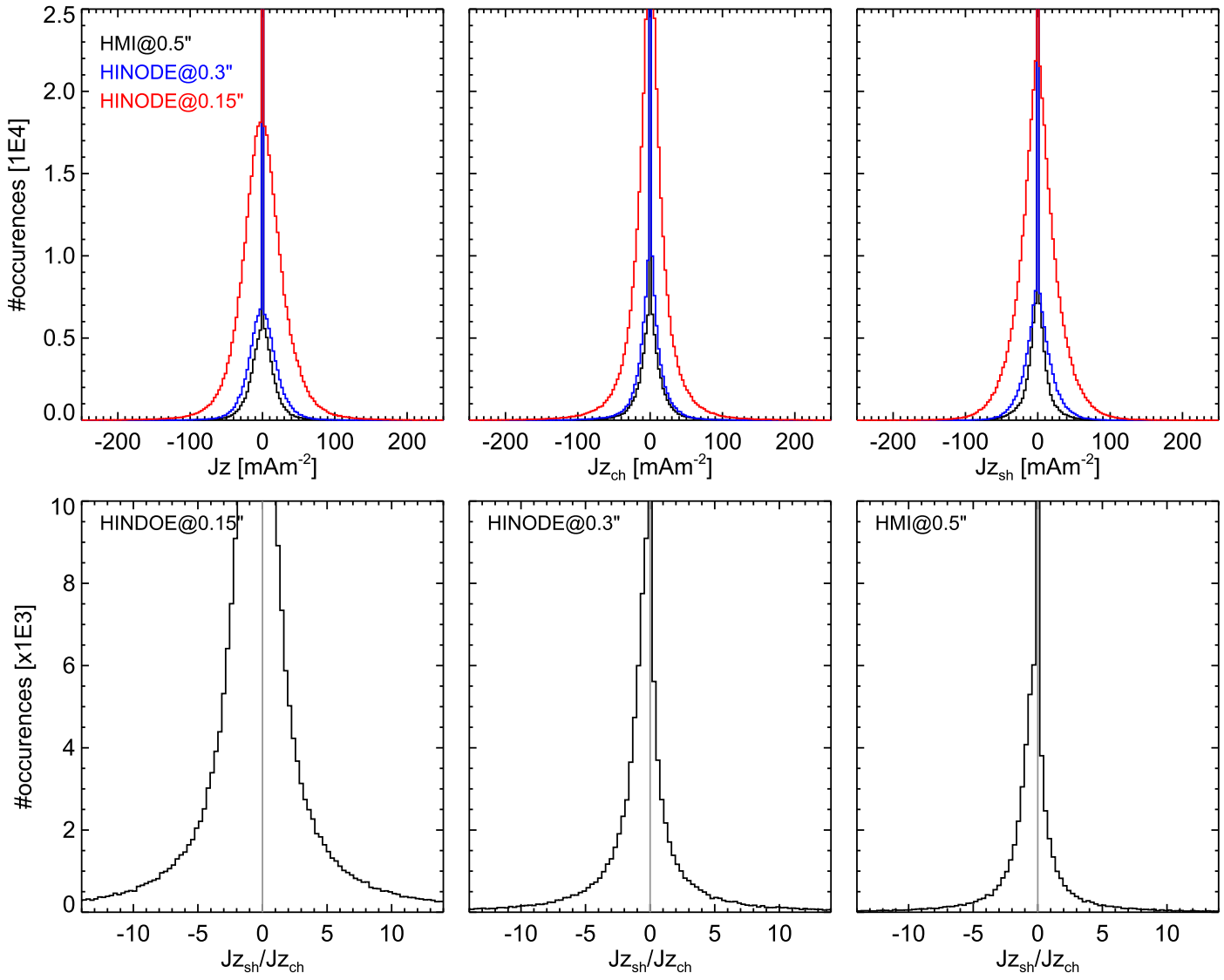

Figure 8. Histograms of J_z (left), Jz_{ch} (middle), and Jz_{sh} (right) distribution at different spatial resolutions of the observing instrument. With an increasing spatial resolution, the area under the histogram enlarges and infers the enhanced field gradients and higher values of current distribution. Bottom row: histograms of the ratio Jz_{sh}/Jz_{ch} with decreasing instrumental resolution. Extended wings and enlarged area under the histogram with spatial resolution implies a greater resolution effect on Jz_{sh} distribution than on Jz_{ch}.

(60%–63%) of shear and twist current remain the same even if the resolution size of the pixel doubled from 0.″3 to 0.″15. Despite the increased resolution, the integrated net quantities from each polarity have no prominent increment. So where can the effect of resolution hide in these estimated quantities of vertical current? We argue that it is the distribution of vertical current components that will be significantly enhanced by the increased instrumental resolution but may not appear in the area averaged quantities. With the increased resolution, the contrast of small-scale fibril features will be better, resulting from an enhanced field gradient. In Figure 8 (top row panels), we show histograms of Jz_{ch} and Jz_{sh} at 0.″5 (AR 11158 observation of HMI), 0.″3 (AR 10930 observation of SOT/*Hinode*), and 0.″15 (*Hinode* observation of SOT/*Hinode* in high-resolution mode). We notice a lower resolution histogram inside the higher resolution histogram of each Jz, Jz_{ch}, and Jz_{sh}.

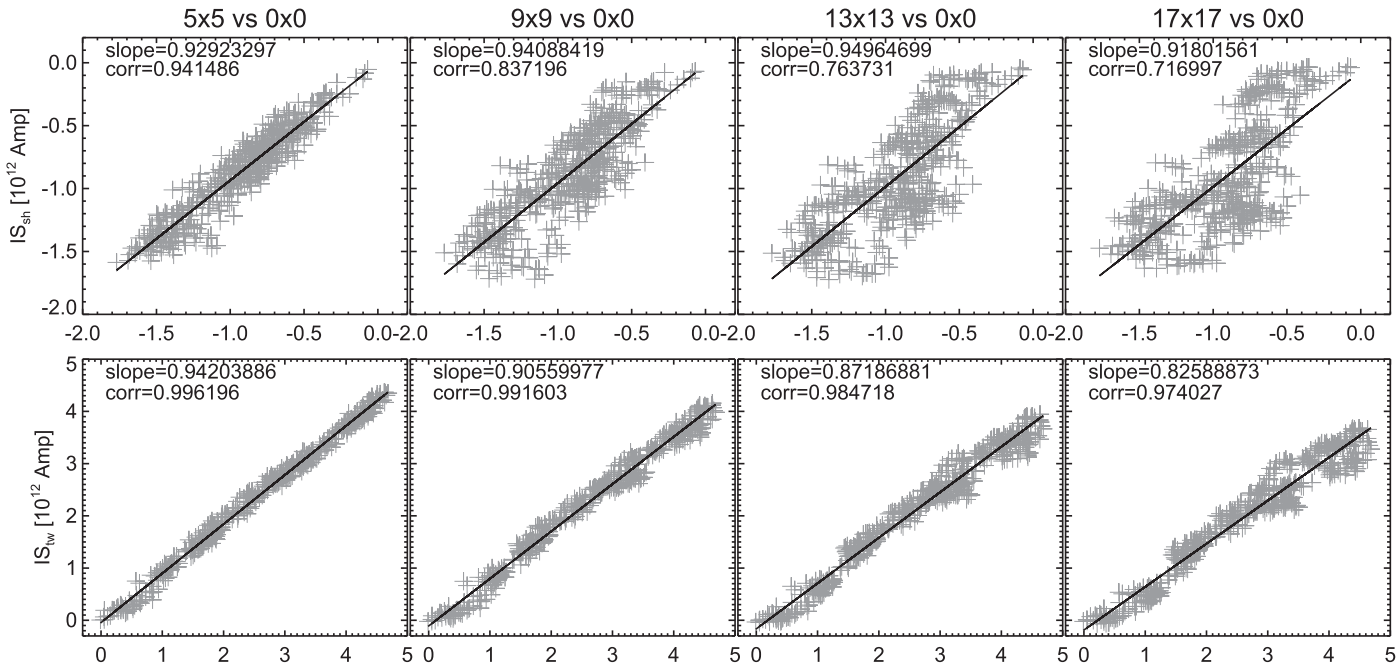

Figure 9. Effect of smoothing on shear and twist currents. The net shear (twist) current of S-polarity in R1 computed at different spatial smoothing windows is plotted against that without smoothing in the top (bottom) row. The scattered data are fitted with a straight line with indicated slope and correlation in each panel. Note that the shear current shows large scatter with poor correlation, the twist current has correlation near to unity.

In the bottom row of panels, we plot the ratio $Jz_{\rm sh}/Jz_{\rm ch}$, which exhibits an enlarged area under the histogram of higher spatial resolution. It implies a greater effect on $Jz_{\rm sh}$ than on $Jz_{\rm ch}$.

4. Discussion

Since the $Jz_{\rm sh}$ is derived from gradients of the field strength, it is more affected by instrumental resolution at which field measurements are acquired. Note that the opposite signed pixels of $Jz_{\rm sh}$ and $Jz_{\rm ch}$ are distributed all over the AR. The $Jz_{\rm ch}$ then seems to be impervious to loss of resolution, indicating that it is a large-scale current. Consequently, the $I_{\rm ch}$ will survive even in the corona as a non-neutralized current, which could explain the twisted or sigmoidal (Canfield et al. 1999) coronal structures. Since the net current is very similar (spatially and temporally) to the twist current, the measurement of the net current, even with limited resolution, will provide a measure of the coronal currents at any time.

The unequal magnitudes of twist and shear currents are likely due to (1) a lack of sufficient spatial resolution and (2) a lack of contribution from other (horizontal) components of the current. In the earlier case, the local distribution of currents severely affected the area averaged value, however, not to that extent. In the latter case, we require vertical derivatives of the fields, which emphasize the requirement of magnetic field observations at multi-heights.

In the case of poor resolution (case 1), the field-free plasma, which is the predicted source of RC and in which the flux tube is surrounded, cannot be resolved. In this case, any flux tube surrounded by similar flux tubes appears as a single entity of flux tube. As a result, the whole sunspot appears as a compact structure. Thus, at a given resolution of the instrument, the net current remains mostly in the form of a twist current with a missing shear current. A consequence that is quite likely is that the twist current is more global and unaffected by spatial resolution, while the shear current is local in origin and more affected by resolution.

To test the above argument, we have computed the twist and shear currents by smoothing the magnetograms by boxcar windows of 5, 9, 13, and 17 pixels and compared with that of no smoothing. If our assumption is correct, at higher smoothing, the twist current must retain its trend, but the shear current must get smeared out. In Figure 9, the net shear current (top row panels) and net twist current (bottom row panels) of S-polarity in region R1 are compared at different smoothing windows with that of no smoothing. The shear current scatters from a fitted straight line more at larger spatial smoothing windows. Also the correlation between the smoothed and unsmoothed ones deviates far from unity (0.94–0.71). However, the twist current retains its trend in the form of a good correlation (0.99–0.97) slope with 18% deviation only. Similarly, we verified and confirmed the same result with other polarities in R2, as well as in the entire AR. Extrapolating these results back to smaller scale features, we can argue that small-scale features hidden within spatial resolution limits might have contributed to the underestimate of the shear current, which in turn fails to cancel the twist current. The investigations by Zhang (2010) also support our interpretations. They found that the individual fibrils are dominated by the current density component caused by magnetic inhomogeneity, while the large-scale magnetic region is generally dominated by the twist component of the electric current density. It should be noted that the smoothing factor we applied, in principle, is the combined result of instrumental resolution capability and the inversion procedure, and may not be equivalent to direct spatial smoothing as applied here. In support of the above thought experiment, we plot the ratio of $Jz_{\rm sh}$ and $Jz_{\rm ch}$ in Figure 8. With the increase of spatial resolution, the occurrences of a ratio value become more toward wings. This means that the numerator $Jz_{\rm sh}$ distribution at any spatial

location becomes more enhanced than that of Jz_{ch} and contributes more to Jz.

5. Summary

The decomposition of the net current reveals that the sign of the Jz_{sh} distribution is opposite that of the Jz_{ch} distribution in about two-thirds of pixels, though smaller in magnitude, and its time profile bears no systematic trend. This result is verified with the high-resolution *HINODE* vector magnetic field. When analyzed the distribution, the opposite signed pixels of shear and twist current density (Figure 3) are located all over the AR. When compared the distribution of Jz and Jz_{ch}, the opposite signed pixels are nondominant and are located mainly at the outer regions of sunspots. These results indicate that the gradient of magnetic field strength majorly contributes to the opposite signed current of that contributed by the curl of the magnetic field direction in the vertical component of current. We conjecture that this observed opposite sign of shear and twist currents is a signature, according to Parker (1996), that the DCs of flux tubes are canceled by their return (sheath) currents. In other words, the current component derived from field strength gradients contributes to sheath or RC of the flux tube.

The degree of net current neutralization in the AR is well above unity due to the presence of sheared PILs. The net value of I_{sh} in AR 11158 is negative in both the polarities, which when added to I_{ch} reduces the DC value in the north polarity, facilitating the near neutrality of the volumetric current. However, it remains to confirm the sign and magnitude of I_{sh} in many ARs and its contribution to neutralization of volumetric currents.

With the increase of spatial resolution, we found higher values of Jz, Jz_{ch}, and Jz_{sh} distribution. However, the resolution effect is more prominent when resolving the field strength gradients and therefore suggests more contribution from Jz_{sh} for the degree of net current neutralization. On the other hand, plasma pressure drops abruptly above the photosphere, allowing for the rapid expansion of a flux tube. As a result, the field strength gradients smooth out to vanishing I_{sh} and the corona remains with volume currents due to twist along the field line.

SDO is a mission of NASA's Living With a Star Program. *Hinode* is a Japanese mission developed and launched by ISAS/JAXA, with NAOJ as a domestic partner and NASA and STFC (UK) as international partners. I thank the referee for specific comments and suggestions that improved the scientific presentation of the content. P.V. is supported by an INSPIRE grant of AORC scheme under the Department of Science and Technology. I am thankful to Prof. P. Venkatakrishnan for introducing me to this problem of net current neutralization.

ORCID iDs

P. Vemareddy https://orcid.org/0000-0003-4433-8823

References

Bobra, M. G., Sun, X., Hoeksema, J. T., et al. 2014, SoPh, 289, 3549
Borrero, J. M., et al. 2011, SoPh, 273, 267
Calabretta, M. R., & Greisen, E. W. 2002, A&A, 395, 1077
Canfield, R. C., Hudson, H. S., & McKenzie, D. E. 1999, GeoRL, 26, 627
Falconer, D. A. 2001, JGR, 106, 25185
Gary, G. A., & Hagyard, M. J. 1990, SoPh, 126, 21
Georgoulis, M. K., Titov, V. S., & Mikić, Z. 2012, ApJ, 761, 61
Hildebrand, F. B. 1974, Introduction to Numerical Analysis (2nd ed.; New York: McGraw-Hill)
Hoeksema, J. T., Liu, Y., Hayashi, K., et al. 2014, SoPh, 289, 3483
Liu, Y., Sun, X., Török, T., Titov, V. S., & Leake, J. E. 2017, ApJL, 846, L6
Parker, E. N. 1979, Cosmical Magnetic Fields: Their Origin and Their Activity (Oxford: Oxford Univ. Press)
Parker, E. N. 1996, ApJ, 471, 485
Ravindra, B., Venkatakrishnan, P., Tiwari, S. K., & Bhattacharyya, R. 2011, ApJ, 740, 19
Schou, J., Scherrer, P. H., Bush, R. I., et al. 2012, SoPh, 275, 229
Sun, X. 2013, arXiv:1309.2392
Suthar, Y., Venkatakrishnan, P., Ravindra, B., & Jaaffrey, S. N. A. 2014, SoPh, 289, 2459
Török, T., Leake, J. E., Titov, V. S., et al. 2014, ApJL, 782, L10
Vemareddy, P., Ambastha, A., & Maurya, R. A. 2012a, ApJ, 761, 60
Vemareddy, P., Maurya, R. A., & Ambastha, A. 2012b, SoPh, 277, 337
Vemareddy, P., Venkatakrishnan, P., & Karthikreddy, S. 2015, RAA, 15, 1547
Venkatakrishnan, P., & Tiwari, S. K. 2009, ApJL, 706, L114
Zakharov, L. E., & Shafranov, V. D. 1986, in Reviews of Plasma Physics, Vol. 11, ed. M. A. Leontovich (New York: Consultants Bureau), 153
Zhang, H. 2001, ApJL, 557, L71
Zhang, H. 2010, ApJ, 716, 1493